ISSN:0971-3093



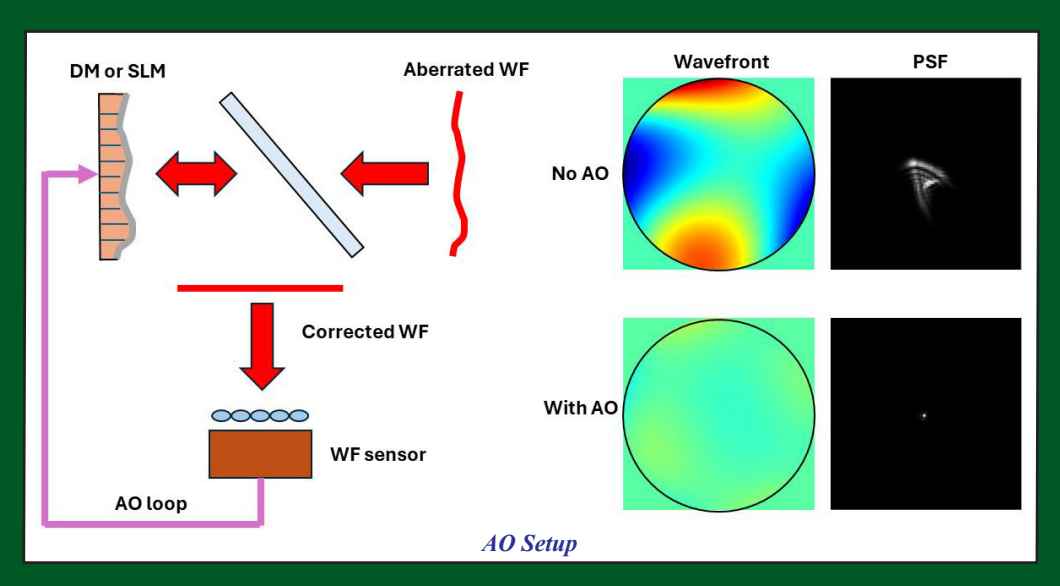
Vol 33, Nos 5 - 6, May - June, 2024

ASIAN JOURNAL OF PHYSICS

An International Peer Reviewed Research Journal

Advisory Editors: W Kiefer, FTS Yu, Maria J Yzuel

Special issue on "Adaptive Optics and Wavefront Sensing"



Guest Editor: Brian Vohnsen



ANITA PUBLICATIONS

FF-43, 1st Floor, Mangal Bazar, Laxmi Nagar, Delhi-110 092, India B O: 2, Pasha Court, Williamsville, New York-14221-1776, USA



Asian Journal of Physics

Vol. 33, Nos 5 & 6 (2024) 309-334





Wavefront sensing and adaptive optics: A Review

Brian Vohnsen

Optics Group, School of Physics, University College Dublin, Dublin 4, Ireland

The propagation of light in vacuum and through homogenous media is governed by diffraction as determined by the wavelength and potential obstacles. In turn, the propagation of light through inhomogeneous media experiences refractive changes that alter the optical path. These accumulated spatial phase variations (i.e. aberrations) are the result of slow spatial refractive index variations and scattering by fast spatial refractive index variations. Aberrations impose small angular deviations in the direction of propagation whereas scattering results in strong angular variations that are highly sensitive to the size of the scattering objects. Large particles scatter mostly in the forward direction while small particles scatter more uniformly. Reflection at a boundary, such as a mirror, occurs due to coherent scattering, while refraction arises from the coherent scattering of wavelets as they enter a medium with a different refractive index. Scattering by large particles as, for example, water droplets in clouds is described by Mie theory, whereas scattering by subwavelength particles as, for example, the N₂ and O₂ molecules of the atmosphere, results in light distributions that are highly dependent on both wavelength and polarization. Aberrations do not describe scattering but rather accumulated slow spatial phase variations that degrade the performance of optical imaging systems. Aberrations can be corrected with careful optical design or with adaptive optics for real-time compensation of aberrations. In this review contribution, the basics of wavefront sensing will be reviewed, some types of wavefront sensors will be described, the commonly used Zernike aberrations will be reviewed, and the operation of common optical active elements to correct for aberrations in real time with adaptive optics will be described. O Anita Publications. All rights reserved.

doi: 10.54955.AJP.33.5-6.2024.309-334

Keywords: Hartmann plates, ray tracing, wavefront propagation, wavefront sensing, Zernike polynomials, Hartmann-Shack sensors, pyramid wavefront sensors, interferometers, guide stars, adaptive optics, deformable mirrors, spatial light modulators, telescopes, microscopes, ophthalmology.

1 Introduction

Wave propagation is governed by Maxwell's equations, which lead to the Helmholtz wave equation that describes the behaviour of light and electromagnetic waves. The journey to our present-day understanding of optics, light propagation, wave models, photons, and vision has not been simple. It is the accumulated efforts of many individuals throughout centuries that have brought us the understanding that we have today [1]. Hence, it is fitting that year 2025 marks the International Year of Quantum Science and Technology [2]. This is celebrated to open new pathways for quantum science as well as to mark a century in quantum physics where optics has been central for many of the early discoveries. The propagation of the wave function, particle spin, Heisenberg uncertainty, and the understanding of the atom, energy levels and the LASER are all closely related to optical concepts that have been known for centuries. We use optics and wave propagation as analogies for advanced physics concepts that can otherwise be hard to visualize. The phenomenon of Young's interference fringes is an excellent example in which light and particle duality can be shown but does require wave propagation for a satisfying understanding. Even for the optics of the

Corresponding author

e mail: brian.vohnsen@ucd.ie (Brian Vohnsen)

eye and perception, it is vital to understand wave propagation across the refractive layers of the ocular medium, before the collapse of the wave function triggered by photon absorption in the visual pigments of the photoreceptor cones and rods. Bohr expressed this clearly in his statement that "owing to the very limits imposed by the properties of light, no instrument is imaginable which is more efficient for its purpose than the eye" [3]. Distributed across the retina, each eye has close to 100 million cone and rod photoreceptors. These cells trigger vision by photon absorption in their visual pigments packed in their outer segments. The cells renew their pigments throughout life at an impressive rate. Children are naturally hyperopic at birth, but the rapid eye growth during the emmetropization process helps bring their vision into focus. Refractive correction will only be required if this process is disrupted. This can be spectacle lenses or contact lenses to correct sphere and cylinder to shift images onto the retina, or it can be personalized wavefront correction with subjective refractive surgery to provide the best possible correction for static aberrations of the eye.



Fig 1. The European Southern Observatory Very Large Telescope ESO VLT at Paranal Observatory, Chile. Credit: ESO/G. Hüdepohl (atacamaphoto.com).

Wavefront sensor technology has its origin in early 20th century astronomy with the invention of the Hartmann plate for the alignment of telescopes and optical quality control [4.5]. Real-time correction of atmospheric aberrations with Adaptive Optics (AO) was proposed later in 1953 by Babcock [6,7]. In 1965, Kogelnik demonstrated that holographic phase conjugation could correct aberrations caused by an inhomogeneous medium through reverse propagation [8]. Yet, owing to the need for rapid wavefront computation in the AO feedback loop, it took several decades before AO became a reality in astronomy at the European Southern Observatory (ESO) in Chile in 1989 [9] and in Hawaii with the Keck observatory in 1999 [10]. Initially, the systems operated with natural guide stars but were soon replaced by an AO laser beacon. This can be appreciated in Fig 1 showing the ESO Very Large Telescope (VLT). Today, to ensure wide field viewing of the sky, it has been necessary to introduce multiple guide stars. For example, the ESO Extremely Large Telescope (ELT) that is currently being constructed in Chile with a 39.3 m primary mirror is expected to have 6 guide stars when ready for observations in 2028 [11]. Another sophisticated telescope in Chile, the Giant Magellan Telescope, will soon be the largest telescope in use when finalized by 2029. It will include 7 primary mirrors each with a diameter of 8.4 m. In all these telescopes, AO systems operate on the smaller secondary mirror. Astronomical AO has been essential for the direct observation of exoplanets [12] and for the capturing of black hole dynamics at the centre of the Milky Way [13]. Some degree of AO is even present in the space-based Webb telescope on the 18 segments of the primary mirror allowing fine tuning of their individual six degrees of freedom whenever misalignments are registered. This is vital to maintain excellent optical performance for as long as possible.

The power of AO in correcting optical aberrations resulted in the development of unique deformable mirrors (DM's) that are costly and challenging to operate. For large telescopes, the performance rather than the price sets the limit. However, DMs at a lower cost began appearing in the late 1990'ies and entered into the areas of vision science, ophthalmology and microscopy. It is likely that such technologies may also appear in low-cost telescopes soon provided that the technology is further refined while lowering the cost.

AO for the human eye had already been proposed by Smirnov in 1961 [14]. At the time, the technology was still not available, but in 1989 Dreher *et al* [15] reported on the use of an active mirror for correction of ocular aberrations in a laser tomographic scanner. In 1997, the first high-resolution AO fundus images were reported by Liang *et al* who used a piezo-actuator-mounted DM [16]. Shortly afterwards in 2001, closed-loop AO for improved vision was realized at a speed of 5 Hz with a low-cost DM by Fernandez *et al* [17]. An example of wavefront capture, and calculated intensity point spread function (PSF) with and without AO for the eye of the present author is shown in Fig 2. Clearly, the wavefront is significantly flattened once the AO-loop has been enabled. To do this in the human eye, an infrared beacon is typically used for the comfort of the subject and to prevent the pupil from contracting if not dilated.

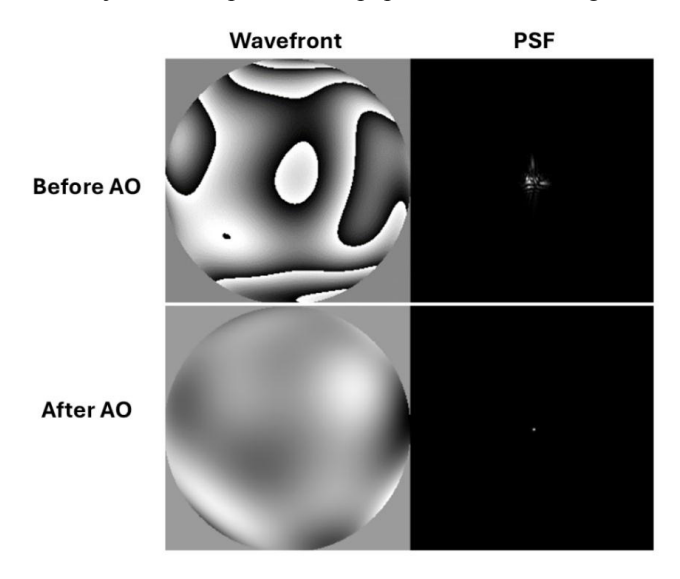


Fig 2. Wavefront (wrapped on 2π) acquired for the author's right eye without and with a low-cost AO system activated across a 6 mm pupil and the corresponding calculated monochromatic point spread function (PSF).

The AO technology provided proof-of-concept that correction could be used not only for improved fundus imaging, but also for potential vision applications with correction of aberrations. Equally, it became clear that it was applicable for real-time vision testing with manipulated amounts and types of aberrations. For example, it is now being used to test the optical performance of refractive or diffractive ophthalmic lens designs in recruited test subjects [18,19]. In imaging, it is being used for direct AO visualization of photoreceptor cones [20-22] and rods in the human retina [23] as well as blood flow and cellular details [24]. It is also being used for the *in-vivo* imaging of animal retinas including those of rodents and monkeys [25-27].

With these advances emerged the integration of improved AO with sophisticated optical imaging systems from fundus cameras (FC) to scanning-light ophthalmoscopes (SLO) and optical coherence tomography (OCT). Undoubtedly, OCT has had the biggest clinical impact with its sectional imaging capabilities that allow for accurate visualization of retinal layers and the impact of retinal diseases [28]. OCT evolved from its similarity with the Michelson interferometer in the time domain, to frequency domain

and swept source OCT that provide high-speed data capture and unprecedented spatial resolution when combined with AO. Yet, AO retinal imaging systems still suffer from a high cost and technical challenges for the operator which has the limited number of commercial systems currently available in the market.

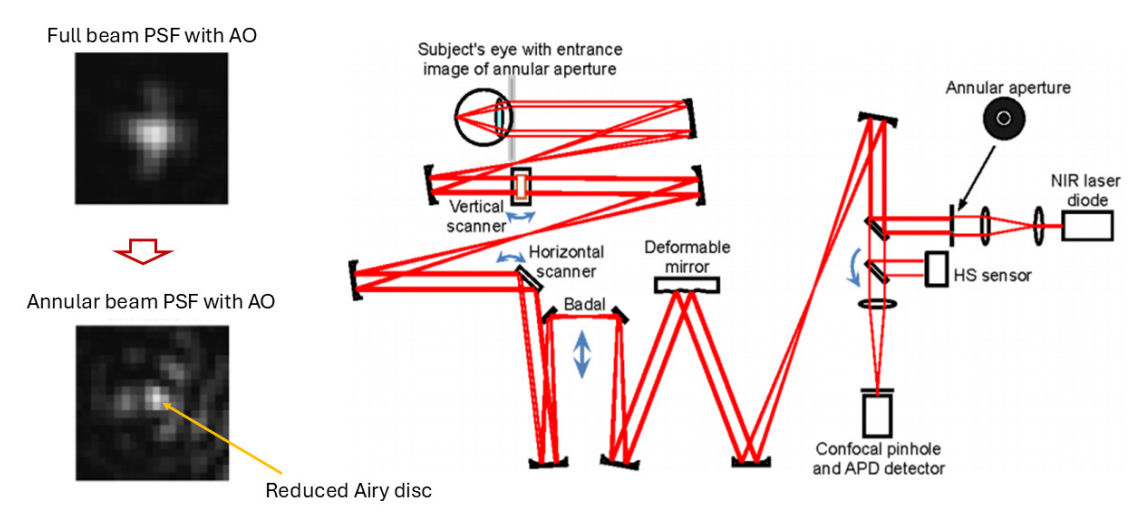


Fig 3. AO-SLO with annular beam used to squeeze down the size of the scanning light probe PSF at focus. The figure has been adapted with permission from [29] © Optical Society of America.

We developed the first annular beam SLO using a Boston MicromachinesTM DM in closed-loop AO and demonstrated a reduction in the central Airy disc of the PSF although this came at the cost of increased ringing outside of the confocal detector [29]. This system is shown schematically in Fig 3 alongside the central Airy disc reduction in the PSF with an annular beam. This method was improved with better AO systems by Sulai and Dubra [30] and recently by Lu *et al* [31] where the smaller PSF allowed for visualization of rods and small retinal structures. AO fundus imaging also added new features by capturing separately the confocal and the non-confocal (scattering) images on using differentials calculated as the difference between two images, for improved contrast [32,33]. This approach of so-called "split detection" has been particularly successful and allowed for improved contrast in retinal images with resemblance to phase contrast microscopy.

Somewhat related, we developed an AO technique with a refractive shallow pyramid conjugated to the eye pupil whereby 4 fundus images are simultaneously captured. The system allows to visualize the retinal cone mosaic but also differences in the pointing direction of the photoreceptors in relation to their scattering characteristics [34]. An example of this is seen in Fig 4. With further refinement, this technology may allow earlier detection of dry age-related macular degeneration (AMD) where the pointing of photoreceptors is altered by the appearance of drusen. These are seen as growing retinal bumps being 10's to 100's of microns across that eventually leads to photoreceptor apoptosis resulting in vision loss or blindness, especially in the foveal region. Currently, this cannot be cured, but technologies are available to translate images outside of the foveal region mostly affected by the disease and thereby regain some degree of vision for affected patients.

Another technology that has progressed significantly is liquid-based tuneable lenses that deform and adjust their optical power in response to an electric current or a movable mechanical element. Such lenses can be modulated rapidly to produce multiple focal points in quick sequential succession [35] which is being used for visual simulation of multifocal lenses. We have used it to drive accommodation in young adults to evaluate the temporal response to defocus stimuli [36]. This study aimed to provide valuable

insights into myopia, as the mechanisms behind emmetropization (the process that keeps retinal images in focus during eye growth) are not well understood. Additionally, it remains unclear how the eye identifies the sign of defocus when encountering visual blur. Our findings suggest that accommodation to a new defocus blur likely involves a conscious decision, given the approximately 100 ms response time needed when other accommodative cues have been effectively removed.

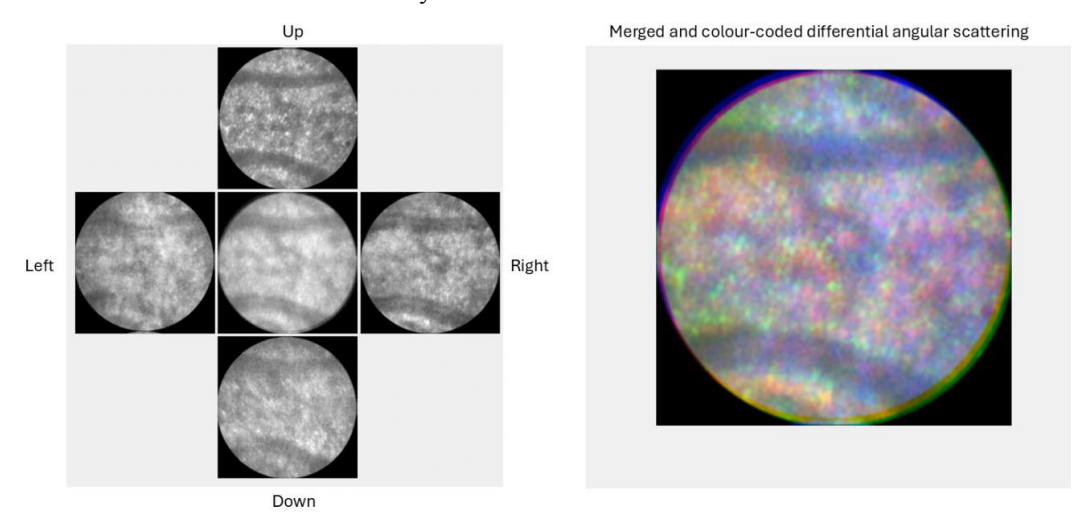


Fig 4. AO-FP images acquired simultaneously through 4 sectors in the eye pupil and from which the local preferred scattering direction and pointing can be determined. The figure has been adapted with permission from [34] © Optical Society of America.

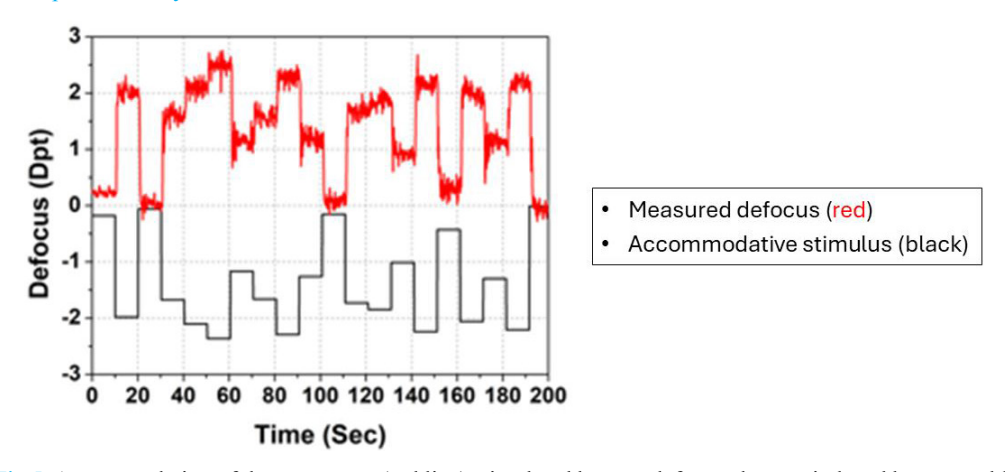


Fig 5. Accommodation of the young eye (red line) stimulated by step defocus changes induced by a tuneable lens (black line). The defocus was determined by use of a fast Hartmann Shack wavefront sensor.

Finally, AO systems were introduced into microscopy allowing for real-time correction of aberrations in biological samples. Defocus and spherical aberrations due to glass slides or coverslips can be corrected with advanced objective lenses, but fluctuating aberrations when imaging inside of cells and in water require more sophisticated techniques, at high numerical aperture (NA) and large imaging depth. In fluorescent imaging, molecules may serve as guide stars themselves where usually a small, but accurate, optical correction is necessary. Such techniques have been developed and used for improved optical imaging in confocal microscopy [37], in multiphoton microscopy [38,39], as well as in stimulated emission depletion microscopy

(STED) and localization microscopy [40-43]. It has also been introduced in widefield microscopy extending the field of view with excellent optical correction.

AO systems that operate using a guide star assume an individual point source in the image plane. This is a good approximation in astronomy when using natural stars, or when using guide stars created with laser beams directed onto the sodium layer in the upper atmosphere at an altitude of approximately 80 – 105 km. At a wavelength of 589 nm, matching the D2a transition of Na atoms, this produces fluorescence serving as guide star beacon. The technology can also be extended to multi-conjugate AO for wider fields of view having multiple sensing and correction elements.

In ophthalmology, a small guide star projected onto the retina is feasible using a narrow ~ 1 mm beam of light at the pupil of the eye. Yet, the retina is not a single layer but multiple cellular layers spanning across a thickness of approximately 300 μ m. The backscattering from these layers observed in the pupil plane is used to determine the ocular aberrations. A two-layer model of the retina is a good approximation, and along with the closed-loop operation of the AO system it can produce a high-quality guide star [44]. For simplicity, a single-layer reflection is commonly assumed, and the error is small.

In microscopy, it is more challenging to generate a suitable small point source due to the high NA. Thus, major efforts have been dedicated to developing blind AO algorithms that optimize a given image metric such as, for example, Michelson contrast or signal strength [45]. More recently, these technologies have been refined with the introduction of deep learning and artificial intelligence (AI). With high computational power AI approaches are particularly encouraging across all fields of AO applications [43,46-48].

Some of the elements used for wavefront sensing and for optical correction and control of aberrations in AO systems are reviewed in the next sections.

2 Optical elements used for sensing of aberrations

Early studies with Hartmann plates were very successful in measuring aberrations. Related techniques have been developed for aberrometry [4] including corneal topography [49,50]. It was recognized that incorporating lenses into Hartmann technology could provide additional benefits. From this emerged a more powerful and versatile sensor, i.e., the Hartmann-Shack (or Shack-Hartmann) HS-WFS [51]. The sensitivity and dynamic range of this sensor is set by the focal length, lenslet pitch, sensor pixel size, and signal-to-noise ratio of the camera detector. It requires an algorithm for sensing the coordinates of each PSF produced by the microlens array. Their coordinate deviations from those obtained with a (typically planar) reference wavefront are determined. It might be tempting to try to focus the light onto single pixels of the sensor. However, spreading the PSF across adjacent pixels enhances sensitivity, as tiny energy shifts between pixels enable sub-pixel resolution. Examples of HW-WFS sensors in our laboratory are shown in Fig 6. The nominal root-mean-square (RMS) sensitivity of the HAS04 sensor is $\lambda/100$ with 100 μ m lenslet pitch whereas the Thorlabs TM sensor is $\lambda/15$ with 150 μ m lenslet pitch.

The coordinates of the PSF produced by each of the lenslets in the array gives a direct measure of the local wavefront tilt in the pupil being sampled. This may be expressed by Eq (1) and Eq (2) for the x- and y-components of the wavefront slope expressed by angles θ_x and θ_y , i.e.,

$$\theta_{x} = \frac{\Delta x}{f} \tag{1}$$

$$\theta_{y} = \frac{\Delta y}{f} \tag{2}$$

where f is the focal length of the lenslets, Δx and Δy are the translations of the PSF coordinates with respect to an unaberrated reference wavefront.

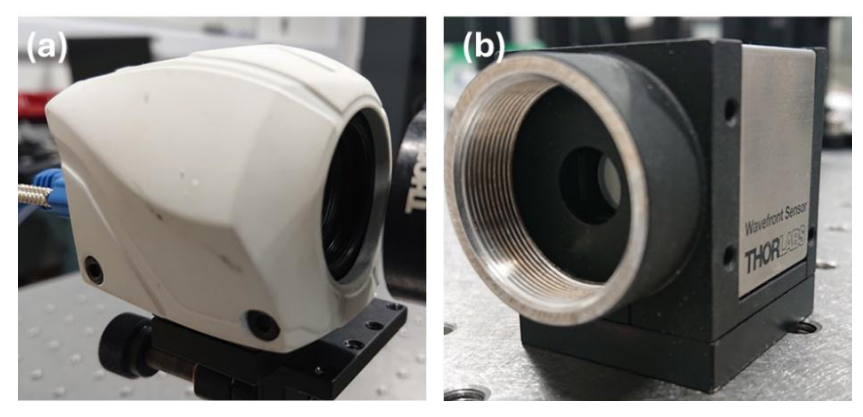


Fig 6. Examples of HS-WFSs in our laboratory (a) HASO4 Imagine EyesTM and (b) WFS-150-5C ThorlabsTM.

Other methods are available to determine optical aberrations. Figure 7 shows schematic diagrams of different common sensors that can be used to measure aberrations of an optical wavefront. These include the HS-WFS, the pyramid wavefront sensor that uses a refractive pyramid (like the one used in Fig 3) to produce 4 images that divide the PSF and reimage them as 4 pupil images [52-55]. Another sensor, the curvature sensor, captures differences in brightness across the wavefront sampled in two (or more) different planes [56]. Brightness variations in the images reveal aberrations from rays propagating at an oblique angle, allowing wavefront reconstruction. Finally, interferometric sensors have very high accuracy but are often challenged by high cost and complications in unwrapping of the interference fringes observed [57].

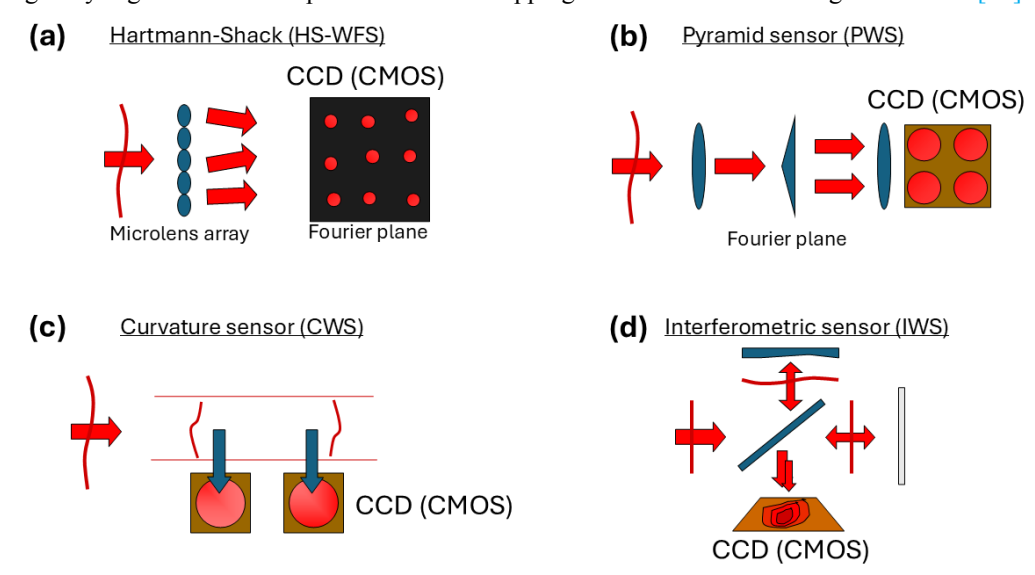


Fig 7. Schematic diagrams of different common sensors used to measure optical aberrations including: (a) HS-WFS, (b) pyramid wavefront sensor, (c) curvature sensor, and (d) interferometric sensor.

Like the curvature sensor, differences in brightness between the pupil images of the pyramid wavefront sensor will be caused by aberrations. The pyramid wavefront sensor is typically time modulated whereby the PSF is scanned across the pyramid apex in a predetermined pattern. In this way, the signal is determined by the time-averaged pupil images. We coded the sensor into a digital spatial light modulator (SLM) that allows for rapid sensor modification and scan pattern coding [55]. An example of this is shown

in Fig 8 and the sensing in Eq (3) and Eq (4) where uniform circular modulation with radius ξ by scanning the pyramid apex with respect to the beam has been included whereby the cartesian derivatives of the wavefront ϕ can be written as,

$$\phi_x = \frac{\xi}{f} \sin\left[\frac{\pi}{2} \times \frac{I_1 - I_2 - I_3 + I_4}{I_1 + I_2 + I_3 + I_4}\right]$$
(3)

$$\phi_{y} = \frac{\xi}{f} \sin \left[\frac{\pi}{2} \times \frac{I_{1} + I_{2} - I_{3} - I_{4}}{I_{1} + I_{2} + I_{3} + I_{4}} \right]$$
(4)

where the four intensity images and wavefront derivatives are calculated pixel-by-pixel (x, y) across the wavefront being sampled [52-55].

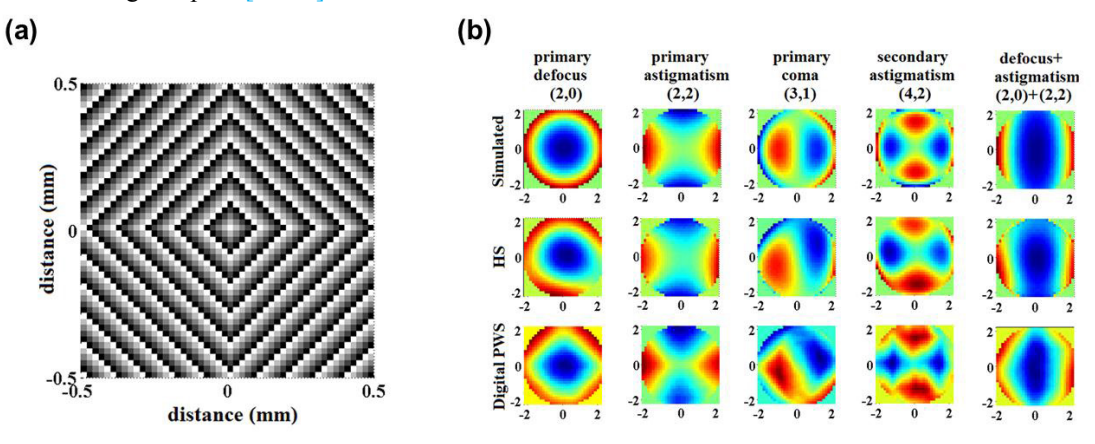


Fig 8. Example of the pyramid wavefront sensor coded into an SLM. In (a) an example of the phase map generated onto the SLM and in (b) comparison between simulated PWS and the measured wavefront with a HS-WFS and PWS, respectively. The figure has been adapted with permission from [55] © Optical Society of America.

A special type of interferometer, the point diffraction interferometer (PDI), has special advantages in that the reference wavefront is generated by a small aperture on the same wavefront. This technique can be used to test ophthalmic lenses [58,59] and can also be realized with an SLM to allow for rapid modifications of its characteristic parameters [60]. Figure 9 shows examples of interferometric images captured with a shallow refractive axicon for PDI sensing of ophthalmic lenses [59]. Here, the apex of the axicon scatters a spherical reference wave that interferes with the wavefront being tested which passes through the conical sides of the axicon.

Often the intensity variations across the wavefront being measured are small. We have utilized this to create wavefront sensors that convert small wavefront variations, and, therefore, aberrations, into intensity gradients. The sensors include a waveguide-based wavefront sensor an a near-resonance sensor using surface plasmon excitation (as a special example of a quasi-resonant sensor). These sensors are described in greater detail in a separate section of this special issue of *Asian Journal of Physics* (see the paper "Sensing wavefront aberrations using intensity gradients"). There, a sequential HS-WFS is also discussed which uses a single lens, instead of a lenslet array, in combination with a digital micromirror device (DMD) to rapidly scan across the wavefront of interest by sampling the PSF coordinates sequentially and rapidly over time [61,62]. This eliminates the risk of potential crosstalk between adjacent cells being sampled (in contrast to the HS-WFS with lenslet arrays where light barriers are frequently used to prevent possible crosstalk). The lenslet array is usually rectangular, but hexagonal arrangements are also practical and beneficial as they better match the typical circular pupil in AO systems.

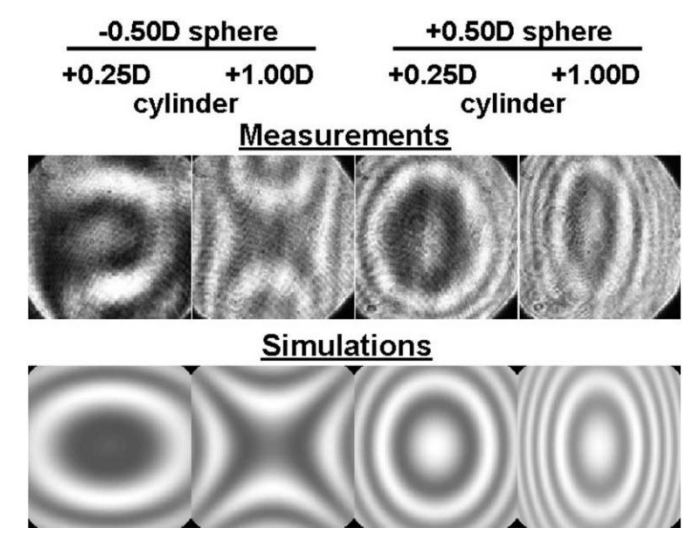


Fig 9. Direct comparison of measured and calculated interferograms obtained with an axicon in a PDI for ophthalmic sphere and cylinder lenses. The figure has been adapted with permission from [59] © Optical Society of America.

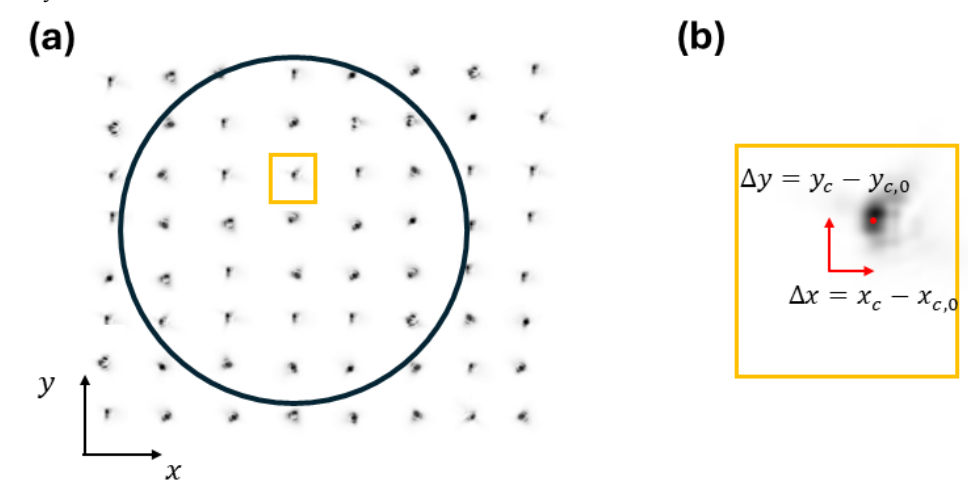


Fig 10. Simulated example of (a) PSF images with a rectangular lenslet array with an HS-WFS and (b) magnified view of one PSF and centroid coordinates. The PSF centroid coordinates are indicated by red arrows and a red dot in the PSF. Note that the intensities are represented on an inverted greyscale to leave the background as white.

For the HS-WFS, it is vital to determine the slope of the wavefront across each sampled microlens in an array. This process is shown schematically with more detail in Fig 10. The image of PSF spots is captured with a charge-coupled-device (CCD) or a complementary-metal-oxide-semiconductor (CMOS). The coordinates of each PSF are determined relative to those obtained using a planar or spherical reference wave. For the determination of the coordinates, the peak location of each PSF across the sensor pixels can be determined. This works well when the PSF is symmetric, but often there will be brightness differences across each PSF and, therefore, a weighting factor may be necessary for the captured intensities across the pixels being exposed to light. An intensity threshold is often used to dampen unwanted background pixel noise. Dim PSF images and ill-defined PSF images, due to poor definition or possible unwanted system

reflections, can be excluded in the subsequent wavefront analysis. Care must be taken to avoid pixel saturation in the sensor as this will distort the determination of the centroid coordinates. Thus, a camera with a high bit depth would typically be preferred for higher accuracy.

With this, the analysis is essentially a refinement of the Δx and Δy used in Eq (1) and Eq (2). The intensity weighted PSF is determined by adding intensities across each PSF as indicated in Eqs (5) and (6). This gives the cartesian coordinates (x_c, y_c) of each PSF. The intensity of each pixel (m, n) in the image is given by $I_{(m,n)}$. The difference between the coordinates affected by aberrations and those unaffected, denoted as $(x_c, y_c)_0$ represents the obliqueness of the probed wavefront across each lenslet in the array.

$$x_{c} = \frac{\sum_{m,n} x_{m,n} I_{m,n}}{\sum_{m,n} I_{m,n}}$$

$$y_{c} = \frac{\sum_{m,n} y_{m,n} I_{m,n}}{\sum_{m,n} I_{m,n}}$$
(6)

$$y_{c} = \frac{\sum_{m,n} y_{m,n} I_{m,n}}{\sum_{m,n} I_{m,n}}$$
 (6)

When the sampled wavefront matches the reference wave, the local obliqueness reduces to zero, i.e., $(\Delta x, \Delta y) = (0, 0)$ for each lenslet and its corresponding PSF in the array. The sampling of the wavefront across the sensor produces a vector of local wavefront slope coordinates with as many components as 2-times the PSF's being sampled (the factor of two is due to the cartesian components of each sampled PSF).

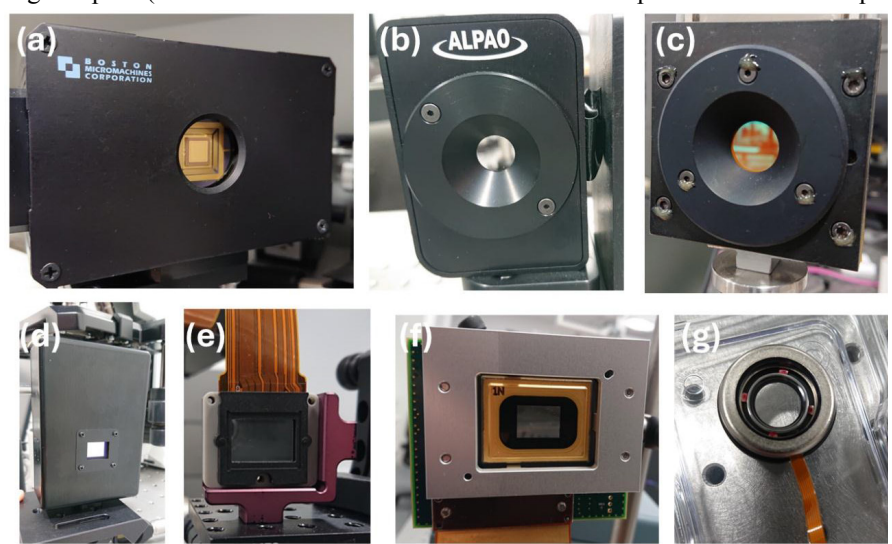


Fig 11. Examples of systems used to control and correct aberrations in our laboratories including (a) MEMS deformable mirror Boston MicromachinesTM, (b) induction-based DM AlpaoTM, (c) induction-based DM MiraoTM, (d) LCOS-SLM HamamatsuTM, (e) HoloeyeTM reflective SLM, (f) DMD (for binary amplitude control) ViALUXTM, and (g) current-driven tuneable lens OptotuneTM.

The systems used for AO correction of wavefront aberrations will typically correct monochromatic aberrations. Wavefront tilt is easily corrected with adjustable planar mirrors, sensor or source realignment. Static defocus and astigmatism can be corrected with spherical and cylindrical corrections. Spherical refraction can be corrected with movable optics. Defocus is easily corrected with an adjustable Badal telescope system [63], with a tuneable lens, or with a deformable mirror, and similar approaches are possible as well for astigmatism. The combination of two elements such as the Alvarez lens or the Lohmann lens [64-67] widens the options to correct variable amounts of aberrations.

Static higher-order aberrations can be corrected with a phase plate, but for real-time AO correction it would normally require either a DM or an SLM that can alter the optical path locally with high accuracy and speed. This adaptive element is typically placed in the pupil plane of the system, although there are alternatives to this approach. Some examples of adaptive systems that can be used for wavefront correction are shown in Fig 11. In turn, chromatic aberrations are usually static and can be corrected by other means, using for example, careful balancing of refractive indices for achromatic designs. Figure 11 includes an example of the DMD that does not directly correct the phase, as it is an amplitude-only device. However, the on/off pixelation of its micromirror array can be used to direct only in-phase components of a wavefront, or as an aperture that scans the wavefront sampled with a point sensor [61,62]. Additionally, a liquid-filled lens is presented as an element solely for adjusting defocus. This design offers the benefits of high-speed operation, low cost, and transmission-based functionality. It should be mentioned that also electrically addressable optofluidic lenses are available that allow for wavefront control of a transmitted wavefront [68,69] much like that of reflective SLMs. These can be fast but have limited corrective range.

Two correctors can also be combined, for example one with large dynamic range but low accuracy, with another adaptive element with higher accuracy but less dynamic range. This is known as woofer-tweeter AO systems [69,70].

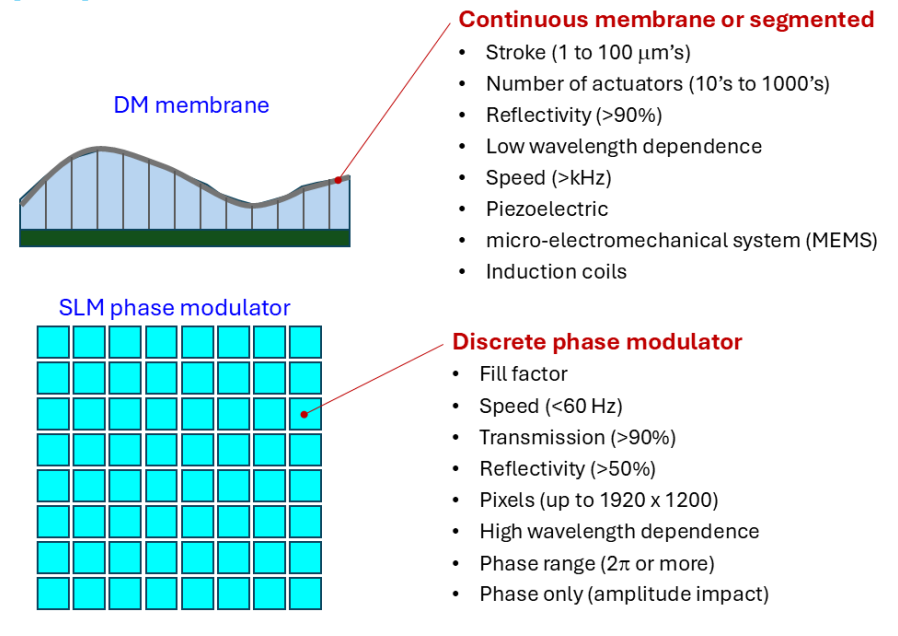


Fig 12. Schematic comparison of the pros-and-cons of DM's with SLM's for phase modulation and AO. Typically, the DM is a continuous surface whereas the SLM is pixelated, wavelength selective and operates at a lower speed.

Schematic drawings of common adaptive technologies with their pros-and-cons are summarized in Fig 12. The DM can either be segmented or consist of a continuous membrane. It will deform in response to electrostatic forces, or due to its physical coupling with piezoelectric actuators or electromagnetic induction coils. The mirrors respond fast to required changes. In turn, the SLMs are slower as they involve liquid crystals. They are sensitive to wavelength through the refractive index and the optical path whether they operate in transmission or reflection. The highest pixel fill factor is usually in reflection whereas in transmission the accompanying circuits limit the fill factor. Due to their periodic structure, they will diffract light. Therefore, it is critical that the phase correction is accurate to limit light in the 0th order diffraction. Alternatively, they can operate in the 1st order diffraction aided by the addition of a blazed grating coded into the SLM image. Both the DM and the SLM have inherent wavefront variations and, therefore, the AO will also actively correct the elements themselves.

DMs are frequently more costly than SLMs. Thus, in many low-cost applications SLMs are attractive, whereas for astronomy the DM technology is preferred due to their speed, light efficiency and wavelength insensitivity. The novel optofluidic electrically addressable lenses [68] (not shown below in Fig 12 deform the lens surface using electrostatic forces, resulting in deformations much like those of the DM membrane in Fig 12.

4 Zernike representation of wavefront aberrations

Traditionally, Seidel aberrations have been used to describe optical aberrations as they provide a clear understanding of the relationship between optical components and ray deviations. Yet, for most modern applications the representation by Zernike polynomials has major appeal and still can be linked back to the classical Seidel aberrations when the error is small.

The wavefront in the pupil plane of the system is typically expressed in polar coordinates due to the circular symmetry of the optical apertures. For monochromatic aberrations the Zernike wavefront notation is widely used. It expresses the wavefront as follows

$$\Phi_{WA}(r,\theta) = \sum_{p} c_p Z_p \tag{7}$$

where c_p is a scaling constant of the individual Zernike polynomials Z_p (with single-index notation) that in combination represent the entire wavefront. Ideally, this summation is an infinite summation series, but typically it can be restricted to include the most predominant terms up to and including the highest order expected. Several different notations have been in use for the ordering of the Zernike polynomials including the Noll notation [71] and the, now more common, ANSI standard [72]. An excellent review article on their properties can be found in Ref [73]. In vision science, they were initially used for ocular aberration sensing, highlighting important aspects of the theory behind the widely used HS-WFS [74,75].

It is common to describe the Zernike polynomials by the combination of a radial polynomial across the pupil for a normalized radius $r \le 1$ and with an angular function for $0 \le \theta \le 2\pi$. This notation results in the following two equations,

$$Z_n^m(r,\theta) = R_n^m(r)\cos(m\theta) \tag{8}$$

$$Z_n^{-m}(r,\,\theta) = R_n^m(r)\sin(m\theta) \tag{9}$$

where $n \ge m \ge 0$. The Zernike polynomials are normalized across the unit circle and are orthogonal functions (i.e., orthonormal basis functions). This means that each term is unique and cannot be represented by a combination of the other terms. if only one term is present in the wavefront it will not add to any of the other terms. However, once the series in Eq (7) is limited and truncated to include a finite number of terms, this uniqueness is no longer satisfied in the wavefront reconstruction. Likewise, if the sensor is slightly displaced off axis, then the sampled wavefront will show as a combination of other terms. Therefore, in practise, it is challenging to determine a unique wavefront and to compare wavefronts directly between different techniques. Frequently, other metrics are being used as; for example, the wavefront root-mean-square (RMS) value which can be expressed through the sum of individual Zernike coefficients.

The Zernike wavefront polynomials are typically divided into low-order aberrations (tilt, defocus, and astigmatism) that can easily be corrected with lenses, and higher-order aberrations (coma, spherical, trefoil, etc.) that require more sophisticated corrections whether static or with AO. When expressed with the single-index ANSI notation the Zernike polynomials Z_p are indexed according to

$$p = \frac{n(n+2) + m}{2}. (10)$$

In this notation, for example defocus is written as Z_4 and spherical aberration is written as Z_{12} . Finally, the Zernike wavefronts can be transformed to non-circular pupils which is of special interest for

oblique illumination [76], for example, when measuring ocular aberrations in relation to the peripheral retina which is highly relevant for myopia research [77]. Individual Zernike polynomials scaled to the full colormap are shown in Fig 13 and ordered with respect to the radial and azimuthal order. Only up to the 4th radial order has been included but commonly also 5th, 6th and even 7th radial order is included in measurements. In general, any arbitrary wavefront will be expressed by a linear combination of individual wavefronts using Eq (7) to scale the contribution of the individual Zernike polynomials.

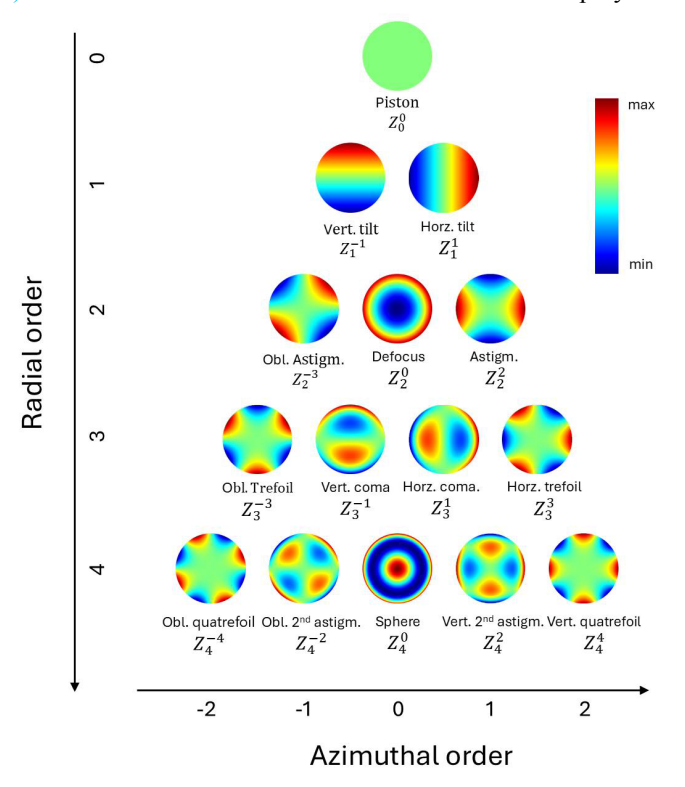


Fig 13. Graphical representation of the Zernike polynomials as a function of radial and azimuthal order.

From the Fourier transform of the wavefront at the pupil, the corresponding intensity PSF images can be calculated. These are shown all scaled equally, in Fig 14 (shown with inverted contrast, i.e., dark is used to represent high intensity).

It is worth noting that even radial Zernike orders correspond to intensity PSFs that have a curved wavefront at focus away from the geometrical image point. In turn, odd radial orders correspond to intensity PSFs that have a planar wavefront (except of sign changes) at focus [78]. This is summarized in Fig 15.

These relate to the wavefront derivatives, i.e., the wavefront slopes, and the Zernike coefficients, and are expressed by the matrix A containing the cartesian Zernike derivatives (not shown in detail here for simplicity, but details can be found in the literature such as, for example, Ref [79]). This relationship between wavefront slopes and Zernike coefficients can be expressed by the following relation:

$$b_{\text{meas}} = A \cdot c \tag{11}$$

where b_{meas} is a vector with the measurements of the wavefront slopes across the total number N of PSFs captured on the sensor, i.e., $(\Delta x, \Delta y)_N$. The vector of Zernike coefficients c_M is truncated by the highest radial order M included in the measurement.

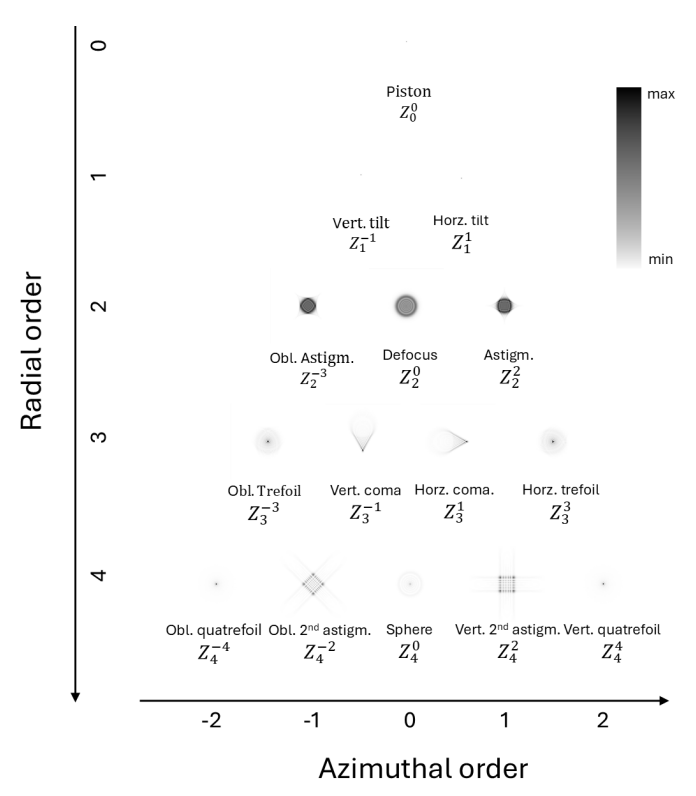


Fig 14. Graphical representation of the PSFs corresponding to individual Zernike polynomials. All PSFs have been printed on the same scale, and, therefore the diffraction-limited focus for piston and tilt is very small. Note that the intensities are represented on an inverted greyscale to leave the background as white.

Zernike polynomials, ANSI notation

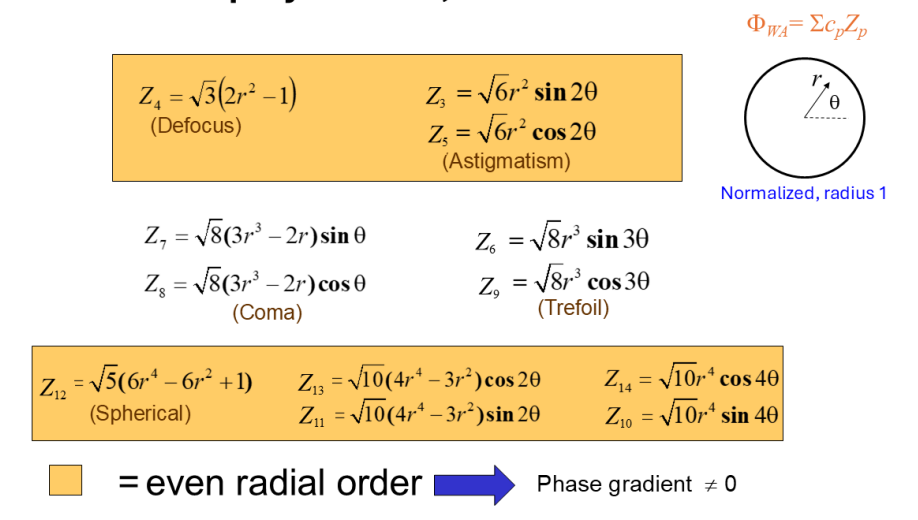


Fig 15. Zernike polynomials with their normalization scaling factors organized as even and odd radial orders and indication of wavefront slope (phase gradient) in the PSF. For simplicity, piston and the two tilt terms have not been included.

To calculate the vector of measured Zernike coefficients Eq (11) must be inverted. Since **A** is not a square matrix this is challenging but the least-square estimate of the wavefront Zernike coefficients c_{est} can be written as

$$c_{est} = [\mathbf{A}^{\mathsf{T}} \mathbf{A}]^{-1} \mathbf{A}^{\mathsf{T}} b_{meas} \tag{12}$$

where A^T is the transposed matrix of A, and $[A^TA]^{-1}$ is the pseudo-inverse of the matrix A. Once this has been done, the measured wavefront can be calculated directly using Eq (7). Typically, the RMS of the wavefront is determined and calculated as

$$RMS = \sum_{p} |c_p|^2. \tag{13}$$

The "peak-to-valley" measurement looks at the highest and lowest points of a wavefront within the pupil area and compares them to an ideal wavefront. It's basically the largest difference between the wavefront's highest and lowest values.

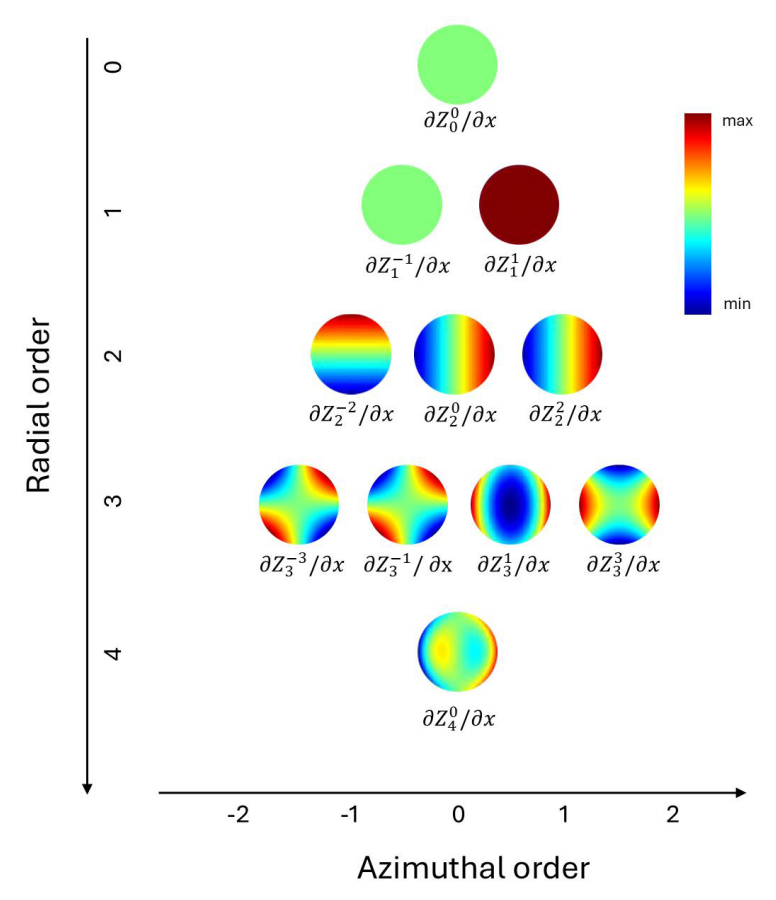


Fig 16. Cartesian x-derivative of the Zernike polynomials needed for the wavefront reconstruction from local slopes. To avoid confusing it with the Zernike polynomials in Fig 13, only up to and including spherical aberration was included here. Thus, for the 4th radial order only the 0th azimuthal order is shown.

5 Adaptive Optics correction of aberrations

With AO correction of the wavefront aberrations, it becomes a matter of relating the phase changes by the corrective device to the deviations detected by the wavefront sensor. Here, the wavefront sensor and

the corrective device are usually located in conjugate planes (projected with 4f lens telescopes or with 4f mirror systems). For a DM, an influence function is first determined by scanning across the DM and poking one actuator at a time. For each of these, a wavefront and a vector of Zernike coefficients is determined. This is then used to obtain the control matrix of the DM. As there is always some error in such a determination, it is often desirable to only correct the wavefront partially at each AO loop iteration until the best correction has been achieved. This provides a temporally stable solution capable of tracking changes, including sudden disturbances, without significantly offsetting the correction. The same holds true when an SLM is used as the corrective device, although here it is possible to apply the full correction in a single step.

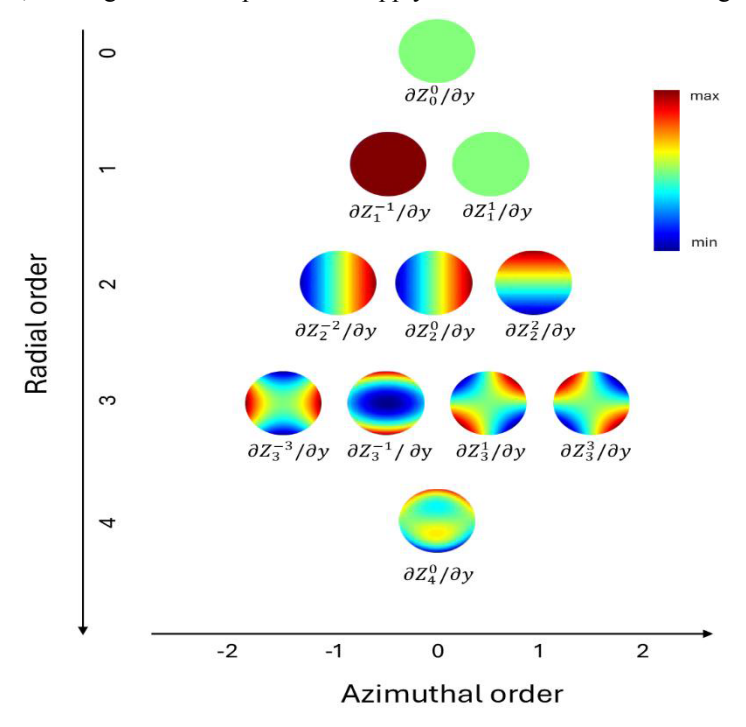


Fig 17. Cartesian y-derivative of the Zernike polynomials needed for the wavefront reconstruction from local slopes. Similar to Fig 16, and to avoid confusing it with the Zernike polynomials in Fig 13, only up to and including spherical aberration was included here. Thus, for the 4th radial order only the 0th azimuthal order is shown.

To speed up the correction process in the closed AO loop it is often desirable to avoid the calculation of the Zernike coefficients and operate directly with the centroid displacements registered by the wavefront sensor. The closed AO loop configuration is illustrated schematically in Fig 18.

A satisfying AO correction is achieved in accordance with the Maréchal criterion [80] when the Strehl ratio is larger than 0.8 corresponding to a wavefront distortion of less than λ 14. The Strehl ratio is determined by the intensity ratios of the measured PSF with respect to that of a diffraction-limited PSF, i.e.,

$$Strehl = \frac{I_{WA\neq 0}}{I_{WA=0}}\Big|_{r=0} \tag{14}$$

Signal-based wavefront sensing that uses a single confocal point-detector and prior knowledge of the sensitivity to aberrations can be used and replace the wavefront sensor in imaging applications. Figure 19 shows one such example with correction of astigmatism using a combination of an SLM with a DM. A point detector is used for the signal-based wavefront sensing and the accuracy can be made very high.

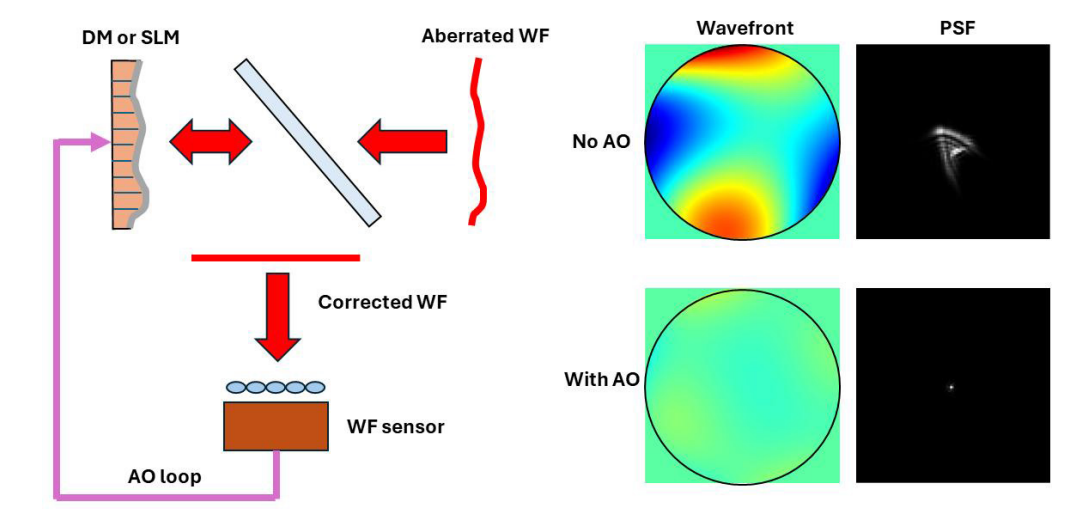


Fig 18. Schematic diagram of closed-loop AO for wavefront correction across a circular pupil.

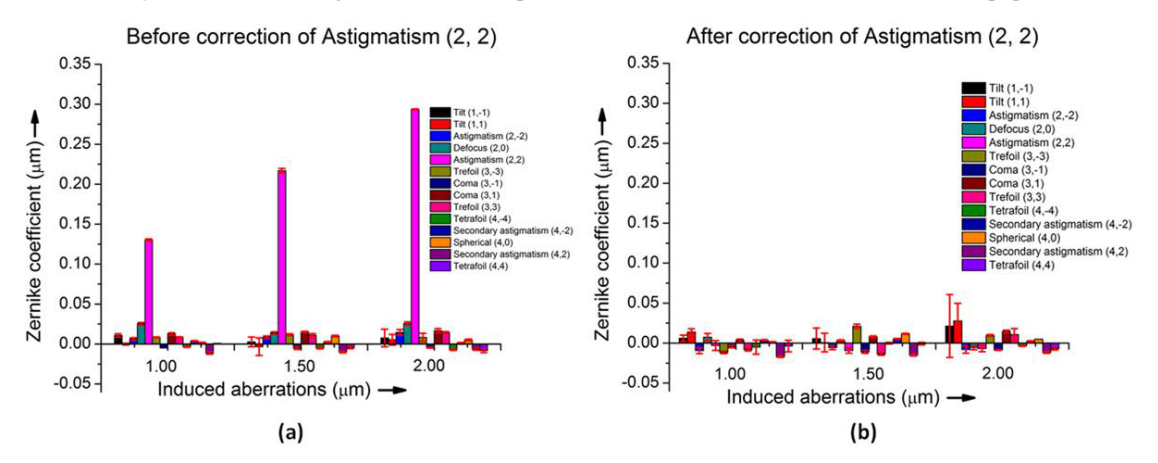


Fig 19. Measurements of induced and corrected aberrations using a combination of DM and SLM. The SLM was used to induce controllable amounts of aberrations (in this case astigmatism) and these were corrected by the DM using a photodiode for signal optimization instead of direct wavefront sensing. The figure has been adapted with permission from Ref [45] © European Optical Society.

Recent progress with AI and deep learning has allowed for training of neural networks for wavefront correction. Although the training process with large datasets is very time consuming, once the training has been completed (provided that the datasets are of high quality) it facilitates wavefront correction and AO correction with excellent performance in microscopy, ophthalmology and astronomy [43,46-48,81-83]. Various methods, such as convolutional neural networks (CNNs), recurrent neural networks (RNNs), and Residual Networks (ResNets), are being explored. Each approach has its own advantages and disadvantages regarding dataset training requirements, speed, and accuracy.

Finally, AO is also being used in the context of light scattering using similar approaches to AI and prior knowledge. Here,SLM's are being used iteratively to gradually compensate for scattering effects to allow imaging or sensing through diffuse scattering media. This process can take many iterations and is therefore not fast, but it holds promise for applications even beyond those of microscopy and ophthalmology [84-87].

6 Ocular aberrations, refractive error, and vision corrections

As discussed in the introduction (Sec 1) wavefront sensing and AO appeared early on for high-resolution retinal imaging with techniques that ranged from fundus cameras to SLO and OCT. The ocular aberrations are commonly expressed in the pupil plane using Zernike polynomials (Sec 4). Yet, more than retinal imaging, people typically know of aberrations and their corrections from visual optics, optometry and ophthalmology. The development of the first spectacle glasses can be traced back to glass work and the late 13th century. Even earlier than that, in the early 9th century reading stones made from transparent hemispheres were being used as magnifiers to help visualize small fonts in religious texts. Both the reading stones and the spectacles were employed to help vision in the ageing eye affected by presbyopia and limited near vision. Convex (positive) lenses were also used as a vision aid for hyperopia, i.e., far-sightedness. Only in the 16th century were concave (negative) lenses being used to treat myopia, i.e., near-sightedness. Benjamin Franklin invented the bifocal spectacle glasses in the late 18th century to allow provide both good far and near vision as dependent on the direction of gaze with higher power when looking down. In the early 19th century a further improvement was made with the invention of trifocal lenses by John Hawkins. The multifocal lenses are available with different optical zone designs in terms of area and shape for near and intermediate vision.

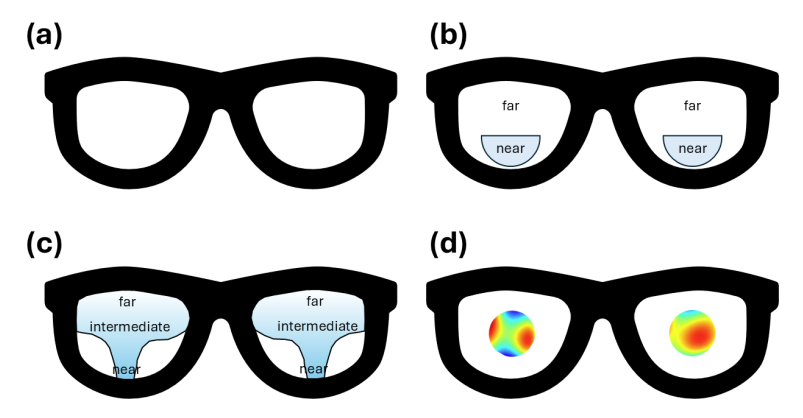


Fig 20. Schematic of different spectacle lenses used for the correction of vision including (a) monofocal, (b) bifocal, (c) varifocal, and (d) waveform-optimized glasses.

Beyond defocus, astigmatism was discovered in the early 19th century by Thomas Young and cylindrical lenses were then used by George Airy to correct it for the eye [88]. Most importantly, Airy developed the first spherocylindrical lenses that even today form the basis of most ocular refractive corrections in terms of sphere and cylinder that relate to the low-order Zernike coefficients Z_2^0 , Z_2^{-2} and Z_2^{-2} . Today's spectacle glasses are more sophisticated and include varifocal (i.e. progressive) lenses invented in 1959 to provide a seamless transition in the central corridor from far to near vision. The downside to this is that there is a certain time of adaptation required as inevitable the optical correction is a compromise between the geometrical shapes realizable and thus there is some image distortion when directing the gaze outside of the central corridor. In the desire to go beyond that, aberrations of the eye can be measured and freeform lenses correcting also higher-order aberrations are possible with waveform-optimized shapes when looking straight ahead. However, once the direction of the gaze is outside of the fully optimized zone vision will be compromised providing a reduction in visual acuity and contract [89]. The different spectacle lenses are shown schematically in Fig 20.

For all of the corrections it is vital that the glasses are centred at each eye so that their performance is as close to the desired correction as possible. They should be worn at the right corneal vertex distance

which is typically in the range of 13 - 17 mm in front of each eye. Prolonged use of low-cost spectacles without careful consideration of intra-pupilar distance can have a negative impact on the eyes both in terms of inappropriate optical correction and eye strain but also in terms of being more susceptible to scratches and inappropriate fitting.

The contact lens dates to early ideas by da Vinci and Descartes, but it was only realized in the late 19th century with a glass scleral lens invented by Fick [90]. Hard contact lenses made of PMMA became common in the mid-20th century but was followed by soft hydrogel contact lenses in the 1970'ies which sparked their widespread use [91]. The contact lenses can also be divided into different zones that allow for good vision at different distances simultaneously. Nevertheless, this is clearly a compromise between the image quality at different distances.

In the mid-20th century also PMMA-based intraocular lenses (IOL's) were developed and used in the treatment of cataracts. Modern IOL's can be divided into zones to provide good vision at various distances and even accommodative IOL's have been introduced that offer some degree of accommodation. To treat presbyopia corneal inlays were invented in the mid-20th century to provide good near vision as a surgical alternative to wearing refractive corrections. The inlays can provide refractive correction or simply use a small aperture to enlarge the depth of focus. The latter is related to recent presbyopia-correcting eye drops that can provide temporary reduction of the pupil size lasting up to a day [92]. An alternative is the use of monovision correction where the dominant eye is corrected for far vision and the non-dominant eye for near vision. The two images perceived are merged by the visual system and an extended depth of focus is perceived that suppresses the undesired blur. Recent developments have focused on developing smart active lenses that can tuneable adjust to different viewing distances from far to near vision. These are typically realized with liquid-filled lenses that can change their optical power quickly in response to an electrical or mechanical signal. The idea is similar to that of autofocus systems used in cameras and can be driven by a camera sensing the defocus adjustment needed.

Refractive surgery plays an equal vital role in correcting of the ocular aberrations. A variety of methods are now available including Photo Refractive Keratectomy (PRK) where the corneal epithelium cellular layer is removed and an excimer laser is used to reshape the cornea and the most common Laser-Assisted In Situ Keratomileusis (LASIK) that since the 1990'ies has become the most common surgical treatment option due to fast recovery time and minimal discomfort [93]. It uses either a keratome or a fs-laser to create a corneal flap that is temporarily flipped to the side to allow for ablation and remodelling of the cornea to correct even higher-order aberrations. Typically around 15 microns of the corneal stroma is removed for each dioptre of correction.

When getting spectacle glasses or contact lenses the required subjective refractive correction is typically determined with a phoropter. This instrument that has been in use the last century uses a range of lenses and prisms to test vision using Snellen letter charts or images. The tests are performed both monocularly and binocularly until a satisfactory subjective correction has been determined. More portable systems that mimic some of the characteristics of the phoropter have been developed while still requiring a user input. This includes handheld devices using smartphones and virtual-reality environments with pattern alignment [94] or colour flicker [95]. To make the process even faster, wavefront sensing methods and autorefractors have been developed that measure the refractive error but they do not match the subjective methods in accuracy. Yet, they are very valuable tools for initial screening and for testing of children where an accurate subjective measurement may not be feasible. Accurate wavefront sensing is also central to the refractive surgery methods to accurately calibrate the correction for the best possible outcome.

In recent years myopia (shortsightedness) has been a particular challenge due to excessive eye growth in young children during early school years where just 1 mm extra axial length will result in 3 dioptres of defocus. Myopia is known to be caused by changed environmental conditions and lifestyle. It

is even predicted that close to 50% of the world population will suffer from myopia by 2050 which is very concerning as some of these will have high myopia where risks of retinal detachment and other retinal complications become increasingly likely [96]. It is known that time spent outdoors is vital to reduce the risk of myopia onset and it is recommended that children spent at least 2 hours outdoors daily [97]. There are many potential reasons for this to be the case, including the release of dopamine in bright environments and changed dioptric demands. This author has also suggested that the smaller pupil size outdoors may play a crucial role as it appears to be matched to the angular acceptance range of the photoreceptors themselves that also continue to change into school years [98]. An indoor pupil is larger, and therefore there is a larger risk that light rays will not travel the full length of each photoreceptor outer segment before possibly leaking out resulting in lower photon capture. Exactly which mechanisms that trigger eye growth remain poorly understood and may involve a combination of factors [99] from the chromatic blur of the eye where blue light focuses in front of the retina but red light focuses behind the retina, the spectral and spatial frequencies, blurred peripheral vision related to hyperopic defocus that pushes the image formation backwards and beyond the retina, and as mentioned the pupil size itself [98].

A number of treatment options are available to try to slow excessive eye growth in children and include low-concentration atropine drops, light treatments from UV (to focus light in front of the retina) and red light (dopamine release as well as reduced pupil size), and a wide variety of myopia control lenses.

Orthokeratology (Ortho-K) lenses are hard contact lenses worn at night to flatten the central cornea and thereby reduce the focusing power of the eye [100]. They are quite effective in doing this and the effect can last for a full day. Under-correction of myopia has also been used to limit axial growth but has proven less effective.

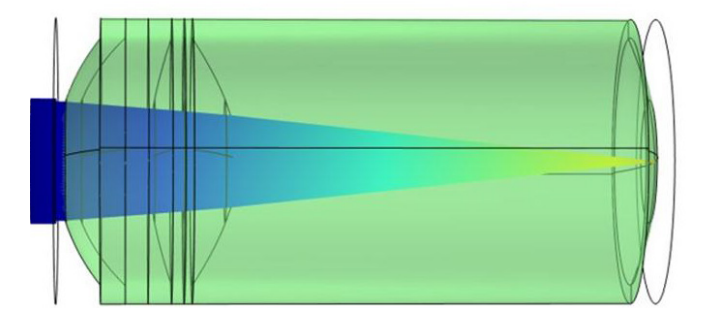


Fig 21. Example of an ocular raytracing model of the human eye using parameters that allow for evaluation of optical performance of refractive corrections. This particular model is based on a model that allows for evaluation of the myopic eye using data from Atchison [104].

Soft multifocal contact lenses have proven effective by creating myopia defocus in the peripheral retina and spectacle glasses that have a large clear central zone in the range of 5-9 mm and either diffusers [101] or add-power in lenslets [102] or zones [103] arranged around the central part of each lens. The latter types of lenses add additional focusing power in the peripheral retina with the aim of removing undesired hyperopic defocus in the peripheral retina. These lenses have proven effective in reducing unwanted axial elongation by more than 50% although it remains an open question if even higher efficacy can be achieved.

In any of the refractive designs for the human eye it is vital to have a good optical model of the eye. An example of such an eye model is shown in Fig 21 using COMSOLTM raytracing. With the model established using accurate ocular data, parts can be altered to test refractive corrections, IOL performance, etc. prior to any clinical assessment and validation. The ocular model in combination with the lenses or refractive corrections gives the designer the optimal tools to tune parameters to accurately predict the image

performance, modulation-transfer characteristics and thereby evaluate the expected improvements to vision. This is equally crucial in the novel myopia control lenses to minimize undesired effects that may cause problems or visual disturbances for the user.

7 Conclusions

We have witnessed AO evolving significantly over approximately 3 decades since its early first use in astronomy [9]. Initially, it was limited by computational power and available corrective elements as well as cost. These factors have all improved vastly and now even low-cost AO can perform well in ophthalmology and microscopy. AO astronomy has provided outstanding results in the search for exo-planets and AO in ophthalmology has enabled the tracking of individual cells and structures in the human retina whereby earlier detection of disease progression has become feasible to facilitate improved treatments.

The latest progress with AI is very encouraging and has opened a new way for optical optimization to approach diffraction-limited performance that is likely going to be vital in improved healthcare within the next decade [105,106]. It potentially overcomes the limitations of the guide star, or guide stars, that is used to optimize most standard AO systems.

Still, the outcome of such progress will have to be compared to what becomes achievable with new low-cost sensing and correction technologies for a more widespread use for example in augmented reality and vision. Such technologies may ultimately be implemented for see-through displays for vision-impaired patients [107] and in advanced eye tracking where accuracy is vital to understand the optical role of saccades and involuntary eye motion to our visual perception [108,109].

Acknowledgements

I wish to thank my present and former students as well as my collaborators and colleagues who have all been essential partners in my learning about wavefront sensing and adaptive optics, fields that have progressed immensely since the turn of the 20th century both technologically and in their applications. I am equally grateful to all the authors who have contributed to this special issue of the Asian Journal of Physics.

References

- 1. Vohnsen B, A short history of optics, *Phys Script*, T109(2004)75–79.
- 2. https://www.quantum2025.org/ (accessed March 1st 2025).
- 3. Bohr N, Light and life, Nature, 131(1933)457-459.
- 4. Hartmann J, Bemerkungen über den Bau und die Justirung von Spektrograpen, Zt Instrumentenkd, 20(1900)47-58.
- 5. Malacara-Hernandez D, Malacara-Doblado D, What is a Hartmann test?, Appl Opt, 54(2015)2296-2301.
- 6. Babcock H W, The possibility of compensating astronomical seeing, Publ Astronom Soc Pacific, 65(1953)229–236.
- 7. Babcock H W, Adaptive optics revisited, Science, 249(1990)253-257.
- 8. Kogelnik H, Holographic image projection through inhomogeneous media, Bell Syst Tech J, 44(1965)2451–2455.
- 9. Rousset G, Fontanella J C, Kern P, Gigan P, Rigaut F, Léna P, Boyer C, Jagourel P, Gaffard J P, Merkle F, First diffraction limited astronomical images with adaptive optics, *Astron and Astrophys*, 230(1990) L29–L32.
- Lyke J E, A quarter century of adaptive optics science operations at Keck Observatory, Proc SPIE 13097(2024)1309770, Adaptive optics Systems IX; doi.org/10.1117/12.3018564.
- 11. https://elt.eso.org/ (accessed March 1st 2025).
- 12. Males J R, Close L M, Guyon O, Morzinski K, Puglisi A, Hinz P, Follette K B, Monnier J D, Tolls V, Rodigas T J, Weinberger A, Boss A, Kopon D, Wu Y, Esposito S, Riccardi A, Xompero M, Briguglio R, Pinna E, Direct imaging of exoplanets in the habitable zone with adaptive optics, Proc SPIE 9148(2014)914820, Adaptive Optics Systems IV; doi.org/10.1117/12.2057135.

13. Ciurlo A, Campbell R D, Morris M R, Do T, Ghez A M, Becklin E E, Bentley R O, Chu D S, Gautam A K, Gursahani Y A, Hees A, O'Neil K K, Lu J R, Martinez G D, Naoz S, Sakai S, Schödel R, The swansong of the galactic center source X7: An extreme example of tidal evolution near the supermassive black hole, The Astrophys J, 944(2023)136; doi.org/10.3847/1538-4357/acb344.

- 14. Smirnov M S, Measurement of the wave aberrations of the eye, Biofizika, 6(1961)687–703.
- 15. Dreher A W, Bille J F, Weinreb R N, Active optical depth resolution improvement of the laser tomographic scanner, *Opt Express*, 24(1989)804–808.
- 16. Liang J, Williams D R, Miller D T, Supernormal vision and high resolution retinal imaging through adaptive optics, *J Opt So. Am A*, 14(1997)2884–2892.
- 17. Fernández E J, Iglesias I, Artal P, Closed-loop adaptive optics in the human eye, Opt Lett, 26(2001)746–748.
- **18.** Piers P A, Fernández E J, Manzanera S, Norrby S, Artal P, Adaptive optics simulation of intraocular lenses with modified spherical aberration, *Invst Ophth Vis Sci*, 45(2004)4601–4610.
- 19. Marcos S, Artal P, Atchison D A, Hampson K, Legras R, Lundström L, Yoon G, Adaptive optics visual simulators: a review of recent optical designs and applications, *Biomed Opt Express*, 13(2022)6508–6532.
- Roorda A, Williams D R, The arrangement of the three cone classes in the living human eye, Nature, 397(1999)520–522.
- 21. Roorda A, Romero-Borja F, Donnelly III W J, Queener H, Hebert T J, Campbell M C W, Adaptive optics scanning laser ophthalmoscopy, *Opt Express*, 10(2002)405–412.
- 22. Drexler W, Fujimoto J G, State-of-the-art retinal optical coherence tomography, *Prog Retinal and Eye Res*, 27(2008)45–88.
- 23. Dubra A, Sulai Y, Norris J L, Cooper R F, Dubis A M, Williams D R, Carroll J, Noninvasive imaging of the human rod photoreceptor mosaic using a confocal adaptive optics scanning ophthalmoscope, *Biomed Opt Express*, 2(2011)1864–876.
- 24. Burns S A, Elsner A E, Sapoznik K A, Warner R L, Gast T J, Adaptive optics imaging of the human retina, *Prog Retin Eye Res*, 68(2019)1–30.
- 25. Wahl D J, Jian Y, Bonara S, Zawadzki R J, Sarunic M V, Wavefront sensorless adaptive optics fluorescence biomicroscope for in vivo retinal imaging in mice, *Biomed Opt Express*, 7(2015)1–12.
- 26. Morgan J I W, Dubra A, Wolfe R, Merigan H, Williams D R, *In vivo* autofluorescence imaging of the human and macaque retinal pigment epithelial cell mosaic, *Inv Ophthalmol Vis Sci*, 50(2009)1350–1359.
- 27. Walters S, Feeks, Huynh K T, Hunter J J, Adaptive optics two-photon excited fluorescence lifetime imaging ophthalmoscopy of photoreceptors and retinal pigment epithelium in the living non-human primate eye, *Biomed Opt Express*, 13(2022)389–407.
- 28. Morgan J I W, The fundus photo has met its match: optical coherence tomography and adaptive optics ophthalmoscopy are here to stay, *Opt Physiol Opt*, 36(2016)218–239.
- 29. Vohnsen B, Rativa D, Ultrasmall spot size scanning laser ophthalmoscopy, Biomed Opt Express, 2(2011)1597–1609.
- **30.** Sulai Y N, Dubra A, Adaptive optics scanning ophthalmoscopy with annular pupils, *Biomed Opt Express*, 20(2012)1647–1661.
- **31.** Lu R, Aguilera N, Liu T, Liu J, Giannini J P, Li J, Bower A J, Dubra A, Tam J, *In-vivo* sub-diffraction adaptive optics imaging of photoreceptors in the human eye with annular pupil illumination and sub-Airy detection, *Optica*, 8(2021)333–343.
- 32. Scoles D, Sulai Y N, Langlo C S, Fishman G A, Curcio C A, Carroll J, Dubra A, *In vivo* imaging of human cone photoreceptor inner segments, *Invest Ophthalmol Vis Sci*, 55(2014)4244–4251.
- **33**. Sredar N, Razeen M, Kowalski B, Carroll J, Dubra A, Comparison of confocal and non-confocal split-detection cone photoreceptor imaging, *Biomed Opt Express*, 12(2021)737–755.
- 34. Qaysi S, Valente D, Vohnsen B, Differential detection of retinal directionality, *Biomed Opt Express*, 9(2018)6318–6330.
- 35. Akondi V, Sawides L, Marrakchi Y, Gambra E, Marcos S, and Dorronsoro C, Experimental validations of a tunable-lens-based visual demonstrator of multifocal corrections, *Biomed Opt Express*, 9(2018)6302–6317.

- 36. Sharmin N, Vohnsen B., Monocular accommodation response to random defocus changes induced by a tuneable lens, *Vision Res*, 165(2019)45–53.
- 37. Booth M J, Adaptive optics in microscopy, *Phil Trans R Soc A*, 365(2007)2829–2843.
- **38.** Bueno J M, Palacios R, Chessey M K, Ginis H, Analysis of spatial lamellar distribution from adaptive-optics second harmonic generation corneal images, *Biomed Opt Express*, 4(2013)1006–1013.
- 39. Booth M J, Adaptive optical microscopy: the ongoing quest for a perfect image, *Light Sci Appl*, 3(2014)e165; doi. org/10.1038/lsa.2014.46.
- **40.** Izeddin I, El Beheiry M, Andilla J, Ciepielewski D, Darzacq X, Dahan M, PSF shaping using adaptive optics for three-dimensional single-molecule super-resolution imaging and tracking, *Opt Express*, 20(2012)4957–4967.
- 41. Lenz M O, Sinclair H G, Savell A, Clegg J H, Brown A C N, Davis D M, Dunsby C, Neil M A A, French P M W, 3-D stimulated emission depletion microscopy with programmable aberration correction, J Biophotonics, 7(2014)29–36.
- 42. Ahn C, Hwang B, Nam K, Jin H, Woo T, Park J-H, Overcoming the penetration depth limit in optical microscopy: Adaptive optics and wavefront shaping, *J Innov Health Sci*, 12(2019)1930002; doi.org/10.1142/S1793545819300027.
- 43. Hu Q, Hailstone M, Wang J, Wincott M, Stoychev D, Atilgan H, Gala D, Chaiamarit T, Parton R M, Antonello J, Packer A M, Davis I, Booth M J, Universal adaptive optics for microscopy through embedded neural network control, *Light Sci Appl*, 12(2023)270; doi.org/10.1038/s41377-023-01297-x.
- 44. Akondi V, Dubra A, Multi-layer Shack-Hartmann wavefront sensing in the point source regime, *Biomed Opt Express*, 12(2021)409–432.
- Jewel A R, Akondi V, Vohnsen B, A direct comparison between a MEMS deformable mirror and a liquid crystal spatial light modulator in signal-based wavefront sensing, *J Eur Opt Soc-Rapid Pub*, 8(2013)13073; doi.org/10.2971/ jeos.2013.13073.
- 46. Paine S W, and Fienup J R, Machine learning for improved image-based wavefront sensing, *Opt Lett*, 43(2018) 1235–1238.
- 47. Nishizaki Y, Valdivia M, Horisaki R, Kitaguchi K, Saito M, Tanida J, Vera E, Deep learning wavefront sensing, *Opt Express*, 27(2019)240–251.
- 48. Ramírez-Quintero J S, Osorno-Quiroz A, Torres-Sepulveda W, Mira-Agudelo A, Experimental wavefront sensing techniques based on deep learning models using a Hartmann-Shack sensor for visual optics applications, *Sci Rep*, 15(2025)9652; doi.org/10.1038/s41598-024-80615-8.
- 49. Campos-García M, Estrada-Molina A, and Díaz-Uribe R, New null screen design for corneal topography, Proc SPIE 8011(2011)801124, 22nd Congress of the International Commission for Optics: Light for the Development of the World; doi.org/10.1117/12.903397.
- **50.** Rodriguez-Rodriguez M I, Gonzalez-Utrera D, Aguirre-Aguirre D, Vohnsen B, Díaz-Uribe R, Corneal topographer using null-screen patterned within a quadrangular acrylic prism, *Opt Continuum*, 3(2023)36–50.
- 51. Shack R V, Platt B C, Production and use of a lenticular Hartmann screen, J Opt Soc Am, 61(1971)656.
- 52. Ragazzoni R, Pupil plane wavefront sensing with an oscillating prism, J Mod Optics, 43(1996)289–293.
- 53. Riccardi A, Bindi N, Ragazzoni R, Esposito S, Stefanini P, Laboratory characterization of a Foucault-like wavefront sensor for adaptive optics, Proc SPIE, 3353(1998)941–951.
- Burvall A, Daly E, Chamot S R, Dainty C, Linearity of the pyramid wavefront sensor, Opt Express, 25(2006)11925– 11934.
- 55. Akondi V, Castillo S, Vohnsen B, Digital pyramid wavefront sensor with tunable modulation, *Opt Express*, 21(2013)18261–18272.
- Campbell H I, Zhang S, Greenaway A H, Restaino S, Generalized phase diversity for wave-front sensing, Opt Lett, 29(2004)2707–2709.
- 57. de Groot P J, A review of selected topics in interferometric optical metrology, *Rep Prog Phys*, 82(2019)056101; doi.org/10.1088/1361-6633/ab092d.
- 58. Acosta E, Chamadoira S, Blendowske R, Modified point diffraction interferometer for inspection and evaluation of ophthalmic components, *J Opt Soc Am A*, 23(2006)632–637.

- 59. Vohnsen B, Castillo S, Rativa D, Wavefront sensing with an axicon, Opt Lett, 36(2011)846-848.
- **60.** Akondi V, Jewel A R, Vohnsen B, Digital phase-shifting point diffraction interferometer, *Opt Lett*, 39(2014) 1641–1644.
- 61. Vohnsen B, Martins A C, Qaysi S, Sharmin N, Hartmann–Shack wavefront sensing without a lenslet array using a digital micromirror device, *Appl Opt*, 57(2018)E199–E204.
- 62. Martins A C, Vohnsen B, Measuring ocular aberrations sequentially using a digital micromirror device, *Micromachines*, 10(2019)117; doi.org/10.3390/mi10020117.
- 63. Badal J, Optometre metrique international. Pour la measure simulanee de la refraction et d l'acuite visuelle meme chez le illetres, Annales d'Oculistique 75(1876)101–117.
- 64. Alvarez L W, Humphrey W E, Variable power lens and system, US Patent, (1970) 3.507.565.
- 65. Lohmann A W, A new class of varifocal lenses, Appl Opt, 9(1970)1669–1671.
- 66. Barbero S, The Alvarez and Lohmann refractive lenses revisited, Opt Express, 17(2009)9376–9390.
- 67. Acosta E, Sasián J, Phase plates for generation of variable amounts of primary spherical aberration, *Opt Express*, 19(2011)13171–13178.
- 68. Banerjee K, Rajaeipour P, A Çağlar, Zappe H, Optofluidic adaptive optics, Appl Opt, 57(2018)6338-6344.
- 69. Mecê P, Bertrand M, Cai Y, Rajaeipour P, Klykov S, Grieve K, Woofer-twetter adaptive optics approach for a compact Full-Field OCT high-resolution retinal imaging over a large field-of-view, Invest Ophthalmol Vis Sci ARVO-abstract 65(2024)3394.
- 70. Lavigne J.-F, Véran J.-P, Woofer-tweeter control in an adaptive optics system using a Fourier reconstructor, *J Opt Soc Am A*, 25(2008)2271–2279.
- 71. Noll R J, Zernike polynomials and atmospheric turbulence, J Opt Soc Am A, 66(1976)207–211.
- Thibos L N, Applegate R A, Schwiegerling J T, Webb R, Standards for reporting the optical aberrations of eyes, *J Ref Surg*, 18(2013)S652–S660.
- 73. Lakshminarayanan V, Fleck A, Zernike polynomials: a guide, J Mod Opt, 58(2011)545–561.
- 74. Liang J, Grimm B, Goelz S, Bille J, Objective measurement of wave aberrations of the human eye with the use of a Hartmann-Shack wave-front sensor, *J Opt Soc Am A*, 11(1994)1949–1957.
- 75. Prieto P M, Vargas-Martín F, Goelz S, Artal P, Analysis of the performance of the Hartmann-Shack sensor in the human eye, *J Opt Soc Am A*, 17(2000)1388–1398.
- 76. Lundström L, Unsbo P, Transformation of Zernike coefficients: scaled, translated, and rotated wavefronts with circular and elliptical pupils, *J Opt Soc Am A*, 24(2007)569–577.
- 77. Jaeken B, Lundström L, Artal P, Fast scanning peripheral wave-front sensor for the human eye, *Opt Express*, 19(2011)7903–7913.
- 78. Vohnsen B, The impact of aberrations in a 3D retinal model eye, Proc SPIE 11814(2021)1181405, Current Developments in Lens Design and Optical Engineering XXII; doi.org/10.1117/12.2594117.
- 79. Tyson R K, Principles of Adaptive Optics, CRC Press, 3rd Edn, (2011).
- 80. Ross T S, Limitations and applicability of the Maréchal approximation, Appl Opt, 48(2009)1812–1818.
- 81. Andersen T, Owner-Petersen M, Enmark A, Image-based wavefront sensing for astronomy using neural networks, *J Astron Telesc Instrum Syst*, 6(2020)034002; doi.org/10.1117/1.JATIS.6.3.034002.
- 82. Soltanian-Zadeh S, Liu Z, Liu Y, Lassoued A, Cukras C A, Miller D T, Hammer D X, Farsiu S, Deep learning-enabled volumetric cone photoreceptor segmentation in adaptive optics optical coherence tomography images of normal and diseased eyes, *Biomed Opt Express*, 14(2023)815–833.
- 83. Zhang L, Zhong L, Guo Y, Gong X, Rao C, Nondeterministic wavefront estimation based on deep learning for multi-band synchronous high-resolution reconstruction technology, *Opt Express*, 33(2025)9224–9245.
- 84. Vellekoop I M, Mosk A P, Focusing coherent light through opaque strongly scattering media, *Opt Lett*, 32(2007) 2309–2311.
- 85. Katz O, Small E, Guan Y, Silberberg Y, Noninvasive nonlinear focusing and imaging through strongly scattering turbid layers, *Optica*, 1(2014)170–174.

- 86. Paudel H P, Stockbridge C, Mertz J, Bifano T, Focusing polychromatic light through strongly scattering media, *Opt Express*, 21(2013)17299–17308.
- 87. Paniagua-Díaz A M, Jiménez-Villar A, Grulkowski I, Artal P, Double-pass wavefront shaping for scatter correction in a cataract's model, *Opt Express*, 29(2021)42208–42214.
- 88. Levene J R, Sir George Biddell Airy, R S (1801-1892) and the discovery and correction of astigmatism, *J Roy Soc London*, 21(1966)180; doi.org/10.1098/rsnr.1966.0017.
- 89. Marchese L E, Munger R, Priest D, Wavefront-guided correction of ocular aberrations: Are phase plate and refractive surgery solutions equal?, *J Opt Soc Am A*, 22(2005)1471; doi.org/10.1364/JOSAA.22.001471.
- 90. Fick A E, Eine Contactbrille, Archiv für Augenheilkunde, 17(1888)279–289.
- 91. Charman, W N, Wavefront technology: past, present and future, Contact Lens & Anterior Eye, 28(2005)75-92.
- 92. Waring IV G O, Price F W (Jr), Wirta D, McCabe C, Moshirfar M, Guo Q, Gore A, Liu H, Safyan E, Robinson M R, Safety and efficacy of AGN-190584 in individuals with presbyopia-The GEMINI 1 Phase 3 Randomized Clinical Trial, *JAMA Ophthalmol*, 140(2022)363–371.
- 93. Pallikaris I G, Papatzanaki M E, Siganos D S, Tsilimbaris M K, A corneal flap technique for laser *in situ* keratomileusis: Human studies, *Arch Ophthalmol*, 109(1991)1699–1702.
- 94. Jeganathan V S, Valikodath N, Niziol L M, Hansen S, Apostolou H, Woodward M A, Accuracy of a Smartphone-based Autorefractor Compared with Criterion-standard Refraction, *Optom Vis Sci.*, 95(2018)1135–1141.
- Rodriguez-Lopez V, Dorronsoro C, Beyond traditional subjective refraction, Curr Opin Ophthalmol, 33(2022)228– 234.
- 96. Holden B A, Fricke T R, Wilson D A, Jong M, Naidoo K S, Sankaridurg P, Wong T Y, Naduvilath T J, Resnikoff S, Global prevalence of myopia and high myopia and temporal trends from 2000 through 2050, *Ophthalmology*, 123(2016)1036–1042.
- 97. French A N, Ashby R S, Morgan I G, Rose K A, Time outdoors and the prevention of myopia, *Exp Eye Res*, 114(2013)58–68.
- 98. Vohnsen B, Geometrical scaling of the developing eye and photoreceptors and a possible relation to emmetropization and myopia, *Vis Res*, 189(2021)46–53.
- 99. Rozema J J, Farzanfar A, Refractive development II: Modelling normal and myopic eye growth, *Ophthalmic Physiol Opt*, 45(2025)120; doi.org/10.1111/opo.13412.
- 100. Bullimore M A, Johnson L A, Overnight orthokeratology, Cont Lens Anterior Eye, 43(2020)322; doi.org/10.1016/j. clae.2020.03.018..
- 101. Laughton D, Hill J S, Wang L, McParland M, Chen Z, Control of myopia using contrast modulation spectacle lenses in a Chinese population: 12-month results, ARVO abstract 66(2025)2815.
- 102. Lam C S Y, Tang W C, Zhang H Y, Lee P H, Tse D Y Y, Qi H, Vlasak N, To C H, Long-term myopia control effect and safety in children wearing DIMS spectacle lenses for 6 years, *Sci Rep*, 13(2023)5475; doi.org/10.1038/s41598-023-32700-7.
- 103. Alvarez-Peregrina C, Sanchez-Tena M A, Villa-Collar C, Martinez-Perez C, Corcuera-Terrero B, Liu N, Li W, Sankaridurg P, Ohlendorf A, Clinical evaluation of MyoCare in Europe (CEME) for myopia management: one-year results; Ophthalmic Physiol Opt, 45(2025)1025–1035.
- 104. Atchison D A, Optical models for human myopic eyes, Vis Res, 46(2006)2236–2250.
- 105. IDC InfoBrief, sponsored by Microsoft, The Business Opportunity of AI: How Leading Organizations Around the World Are Using AI to Drive Impact Across Every Industry, IDC #US51364223, Nov. 2023 (see: https://blogs.microsoft.com/blog/2024/03/11/microsoft-makes-the-promise-of-ai-in-healthcare-real-through-new-collaborations-with-healthcare-organizations-and-partners/).
- 106. Fauw J D, Ledsam J R, Romera-Paredes B, Nikolov S, Tomasev N, Blackwell S, Askham H, Glorot X, O'Donoghue B, Visentin D, van den D G, Lakshminarayanan B, Meyer C, Mackinder F, Bouton S, Ayoub K, Chopra R, King D, Karthikesalingam A, Hughes C O, Raine R, Hughes J, Sim D A, Egan C, Tufail A, Montgomery H, Hassabis D, Rees G, Back T, Khaw P T, Suleyman M, Cornebise J, Keane P A, Ronneberger O, Clinically applicable deep learning for diagnosis and referral in retinal disease, *Nat Med*, 24(2018)1342–1350.

107. Kartha A, Sadeghi R, Bradley C, Tran C, Gee W, Dagnelie G, Measuring visual information gathering in individuals with ultra low vision using virtual reality, *Sci Rep*, 13(2023)3143; doi.org/10.1038/s41598-023-30249-z.

- 108. Adhanom I B, MacNeilage P, Folmer E, Eye tracking in virtual reality: a broad review of applications and challenges, *Virtual Real*, 27(2023)1481–1505.
- 109. D'Angelo J, Rodriguez R, Reeves S, Otero-Millan J, Measuring upright perception and torsional eye position in virtual reality, *J Vision VSS-abstract*, 22(2022)3817; doi.org/10.1167/jov.22.14.3817.93.

[Received: 15.06.2024; revised recd: 28.06.2024; accepted: 30.06.2024]